1   # Body saccades of *Drosophila* consist of stereotyped banked turns

2   **Florian T. Muijres[1,2,*], Michael J. Elzinga[1], Nicole A. Iwasaki[1], Michael H. Dickinson[1,3]**

3   [1] University of Washington, Seattle, WA, USA

4   [2] Experimental Zoology Group, Wageningen University, Wageningen, the Netherlands

5   [3] Current address: California Institute of Technology, Pasadena, CA, USA

6   ***Corresponding author. E-mail: florian.muijres@wur.nl**

7

10

11   **SUMMARY**

12   The flight pattern of many fly species consists of straight flight segments interspersed with rapid

13   turns called body saccades, a strategy that is thought to minimize motion blur. We analyzed the

14   body saccades of fruit flies (*Drosophila hydei*), using high-speed 3D videography to track body

15   and wing kinematics and a dynamically-scaled robot to study the production of aerodynamic

16   forces and moments. Although the size, degree and speed of the saccades vary, the dynamics of

17   the maneuver are remarkably stereotypic. In executing a body saccade, flies perform a quick roll

18   and counter-roll, combined with a slower unidirectional rotation around their yaw axis. Flies

19   regulate the size of the turn by adjusting the magnitude of torque that they produce about these

20   control axes, while maintaining the orientation of the rotational axes in the body frame constant.

21   In this way, body saccades are different from escape responses in the same species, in which the

22   roll and pitch component of banking is varied to adjust turn angle. Our analysis of the wing

1

23 kinematics and aerodynamics showed that flies control aerodynamic torques during the saccade

24 primarily by adjusting the timing and amount of span-wise wing rotation.

25

26   **INTRODUCTION**

27 When exploring a local environment, many species of flies exhibit a flight pattern consisting of

28 straight segments interspersed with rapid turns called body saccades (Collett and Land, 1975;

29 Tammero and Dickinson, 2002; Wagner, 1986; Wehrhahn et al., 1982). This distinct flight

30 pattern might serve many functions, but one likely advantage is that the quick turns allow flies to

31 restrict the time periods during which their visual system is severely compromised by motion

32 blur (Collett and Land, 1975; Hateren and Schilstra, 1999; Land, 1999; Schilstra and Hateren,

33 1999). Whatever the function, it appears to be the preferred means of changing direction in some

34 species. For example, a recent analysis of *Drosophila melanogaster* found that more than 80% of

35 all changes in heading occur via body saccades (van Breugel et al., 2012).

36   There is some controversy regarding the neural mechanisms that trigger saccades in

37 *Drosophila* (Dickinson, 2014). Several studies of both free and tethered flight behavior suggest

38 that most saccades are triggered by visual expansion and thus represent collision avoidance

39 reflexes that protect flies from flying into large obstacles or avoiding clutter (Censi et al., 2013;

40 Reiser and Dickinson, 2013; Stewart et al., 2010; Tammero and Dickinson, 2002). Other studies,

41 however, suggest that some saccades are triggered internally by a deliberately stochastic process

42 that functions to optimize the animal's search efficiency (Maye et al., 2007; Reynolds and Frye,

43 2007). In addition, flies exhibit rapid turns in other contexts, such as when they lose contact with

44 an odor plume (van Breugel and Dickinson, 2014), or in response to a rapid visual expansion as

45 might be created by an approaching predator (Muijres et al., 2014). It is not known, however,

46 whether rapid turns elicited by different stimuli or internal triggers operate via a single common

47 motor program.

48   The aerodynamic basis of saccades, which is the main subject of this paper, has been

49 investigated previously by Fry and coworkers using the fruit fly, *Drosophila melanogaster* (Fry

50 et al., 2003). Based on a relatively small number of high speed video sequences, these authors

51 proposed a model in which flies change course primarily by creating torque around their yaw

52 axis (defined in that study as perpendicular to the longitudinal body axis), which they accomplish

53 by simultaneously changing stroke amplitude and deviations out of the stroke plane. In addition,

54 these authors reported that the changes in wing kinematics were biphasic, which they interpreted

55 as indicating that flies generate first torque and then counter-torque during each maneuver.

56 Finally, they presented a simple model in which the dynamics about the yaw axis were

57 dominated by inertia during the brief maneuvers, consistent with the production of counter-

58 torque (Fry et al., 2003). Subsequent authors, however, challenged some conclusions of this

59 simple model. Hesselberg & Lehmann (2007) noted that due to the reciprocating pattern of wing

60 motion, the damping about the yaw axis is quite large and should quickly dominate dynamics

61 during turns – a calculation that was supported by subsequent models and measurements (Cheng

62 et al., 2010; Dickson et al., 2010). Hedrick and coworkers (Hedrick et al., 2009) went so far as to

63 suggest that animals over a very large size range need only produce a small amount of counter-

64 torque during saccades, and can rely primarily on passive damping to coast to a stop after

65 initiating a turn. Further, studies of corrective maneuvers in *Drosophila* suggested that flies

66 generate yaw torque by regulating the angle of attack of the wing during the upstroke and

67 downstroke, and not by altering either stroke amplitude or stroke deviation (Bergou et al., 2010).

68   In this paper, we employed 3D high-speed videography to capture the wing and body

69   motion of the fruit fly, *Drosophila hydei*, during free flight body saccades. Although this study

70   repeats the basic paradigm developed by Fry and coworkers over a decade ago (Fry et al., 2003),

71   the improvements in high speed cameras as well as the utility of an automated machine vision

72   tracking system allowed us to revisit saccade dynamics with greater resolution and statistical

73   rigor. The results demonstrate that body saccades are a remarkably stereotyped behavior

74   combining a brief banked turn (requiring rotation and counter-rotation in roll and pitch) with a

75   unidirectional rotation about the yaw axis. By measuring the changes in wing motion during

76   saccades and using a dynamically-scaled robot, we were able to determine the relative

77   importance of different features of wing motion in generating forces and torques. The results

78   help to resolve some of the recent controversies regarding the dynamics of saccadic turns in

79   *Drosophila* and other insects.

80

81   **RESULTS**

82   We tracked a total of 44 flight sequences (Fig. 1, see Materials and Methods), each

83   consisting of a straight flight segment followed by a single body saccade (see Supplementary

84   Movies S1,S2). Assuming that there is no difference between left and right hand turns, we

85   mirrored all left hand turns, and then aligned all sequences based on time and heading with

86   respect to the start of the saccade (Fig. 1E,F, see also Supplementary Movies S3-S6). Heading is

87   defined as the angular direction of the flight path, not the body orientation. The saccadic turn

88   angles ($\Delta\sigma$), which quantify the total angular change in heading, varied substantially among

89   saccades from approximately 20° to almost 180° (Fig. 1E,F, Fig. 2A,B), with an average of

90   93°±27° (mean±s.d., n=44). During the maneuvers, flight speed tended to dip briefly and then

91   gradually rise (Fig. 2C). The duration of turn ($\Delta t = t_{stop}$-t_{start}) was 49 ±18 ms (n=44), or

92   approximately 9 wingbeats, although this is an underestimate of the entire maneuver because t_{start}

93   and t_{stop} were defined using finite thresholds (see Materials and Methods). These basic saccade

94   metrics are similar to those previously reported on free flying *D. melanogaster* (Tammero &

95   Dickinson 2002; Frye et al., 2003; van Breugel et al. 2012).

96   To examine how flies alter heading during saccades, we measured the magnitude and

97   direction of horizontal and vertical accelerations throughout the maneuver (Fig. 2D-F).

98   Immediately at the start of the saccade, flies generate a horizontal force that results in a sideways

99   acceleration. The magnitude (a_{hor}/g) of this sideways acceleration first increases and then

100   decreases (Fig. 2E), while its orientation (σ_a) remains relatively constant (Fig. 2D). Vertical

101   acceleration (a_z/g) remains near zero throughout the entire maneuver (Fig. 2F).

102   The time course of roll rate, pitch rate, and yaw rate during the maneuvers (Fig. 1C, 2G-I)

103   along with their integrals and derivatives (Fig. S1) show that flies rotate about all principal body

104   axes, and thus body saccades constitute a banked turn. Flies also increase force production so the

105   vertical component remains roughly equal to body weight (Fig. 2J,F). The orientation of *F* in the

106   body reference frame remains constant (Fig. 2K,L), consistent with the so-called 'helicopter

107   model' of insect flight (David, 1978; Götz and Wandel, 1984). Thus, as with more rapid escape

108   maneuvers (Muijres et al., 2014), a fly generates sideways accelerations during saccades by

109   rotating its body rather than by adjusting the orientation of the force vector in the body frame.

110   To determine how the flies control roll, pitch and yaw throughout the saccade, we

111   estimated torque about these axes as the sum of torque required to overcome inertia (inertia

112   torque) and torque required to overcome damping (damping torque) (Fig. 3, see Eqn 2 in

113   Materials and Methods). Torque about the yaw axis consists mostly of damping torque

114   confirming that yaw rotations during a saccade are highly damped (Hedrick et al., 2009;

115   Hesselberg and Lehmann, 2007). In contrast, torque about the roll axis consists about equally of

116   inertial torque and damping torque, whereas damping torque about the pitch axis is negligible

117   compared to inertial torque. The fact that rotations about the pitch axis are poorly damped during

118   saccades is supported by a recent study of forward flight dynamics in fruit flies (Elzinga et al.,

119   2014).

120   A simple means of implementing a banked turn would be to rotate the body about a fixed

121   axis in the stroke plane and then to counter-rotate to continue level flight, while at the same time

122   generating a yaw rotation to align body orientation with the new flight heading. The magnitude

123   of the turn could then be adjusted by regulating the amount of torque produced, and not its

124   direction. Evidence that flies might implement such a simple control scheme is shown in Fig. 4.

125   The torque vectors for the primary rotation phase and the counter-rotation phase for all 44

126   sequences (in blue and orange, respectively) aligned remarkably well (Fig. 4A,B). The average

127   torque vector axes for the initial rotation and counter-rotation are defined as the primary torque

128   axis μ_1 and the counter-torque axis μ_2, which are oriented 36° and 8° from the longitudinal body

129   axis, respectively. The time history of the direction (Fig. 4A) and magnitude (Fig. 4C,D) of the

130   torque component in the stroke plane exhibits a biphasic shape indicative of rotation and counter-

131   rotation about the μ_1 and μ_2 axis, respectively (Fig. 4C). In contrast, little torque is generated

132   about the orthogonal axes ($\mu_{1\perp}$ and $\mu_{2\perp}$, respectively, Fig. 4D; see also Fig. S2). Thus, animals

133   execute the banked turn by generating torque and counter-torque about two control-axes (μ_1 and

134   μ_2) whose orientation remains constant from saccade to saccade (Fig. 4A,B). The magnitude of

135   the torque produced about the control axes, however, does correlate with the turn angle (Fig 4F),

136   which suggests the mechanism by which flies regulate the size of the heading change.

137   Simultaneously with the rotations about the μ_1 and μ_2 axes, but within a longer time

138   scale, flies generate a unidirectional yaw torque in the same direction as the change in heading

139   (Fig. 4E). Also, the magnitude of mean yaw torque during the turn is positively correlated with

140   turn angle (Fig. 4H). Although not necessary for changing the direction of the flight path, the

141   yaw rotation is required to align the longitudinal body axis with the new heading. This correction

142   to minimize sideslip is not fully completed in most sequences due to limitations of our

143   visualization volume (Fig. 4E). Note that by rotating about the yaw axis while its body is banked,

144   the fly will generate a head down movement within the world frame of reference. This could

145   explain why the initial body rotation axis μ_1 and counter-rotation axis μ_2 are not aligned and that

146   μ_2 includes a smaller pitch (down) component.

147   The sequence of 21 averaged wingbeats (n=44 trials) show that all kinematic parameters

148   (wingbeat frequency, stroke angle, deviation angle, and wing rotation angle, Fig. 1C) change

149   during a saccade, and that these modifications are all very subtle (Fig. 5A-G). Wingbeat

150   frequency increases by only a few Hz and all modifications in wing angles are less than 5°.

151   Nevertheless, replaying the averaged kinematic sequence on the robotic fly generated normalized

152   forces ($|\mathbf{F}|$) and torques (T_{roll}, T_{pitch} and T_{yaw}) that were similar to those estimated from body

153   dynamics (using Eqns 1-2 in Materials & Methods, respectively, Fig. 5H-K). For example, the

154   time history for the moment about the roll axis measured on the robotic fly exhibits the torque

155   and counter-torque that is predicted from body dynamics (Fig. 5I). Thus, although the measured

156   changes in wing motion are subtle, they appear sufficient to capture the requisite changes in

157   forces and moments reasonably well. Because the robotic fly is fixed and cannot translate and

158   rotate in response to the forces and moments it generates, we did not expect (nor obtain) a perfect

159   match between the measured forces and moments and those calculated from body dynamics.

160   To better understand how flies modulate wingbeat kinematics to control torque around

161   each individual control axis during a saccade, we extracted the wing kinematics associated with

162   peak torque about the μ_1, μ_2, and yaw axes from the entire dataset and replayed these kinematics

163   on the robotic fly (Fig. 6, see Materials & Methods). The kinematics correlated with peak torque

164   production exhibit distortion of all three wing angles (Fig. 6A-C), and when played through the

165   robot, produced the expected torques (Fig. 6D-F). The fly's wing motion is able to create

166   positive yaw torque throughout almost the entire wingbeat, with the exception of brief periods

167   during stroke transitions (Fig. 6D). In contrast, torque production about the μ_1 and μ_2 axes is

168   more complicated in that the time history includes both positive and negative excursions and the

169   magnitude of the transient peaks are quite large relative to the average value (Fig. 6E). Most of

170   the variations in torque production relative to the torque generated by the steady flight wingbeat

171   (i.e. the symmetric wingbeat that produced weight support and no net torque, Fig 1D), occur at

172   the start of the upstroke and downstroke, just after stroke reversal (Fig. 6E). The wingbeat

173   patterns that generate peak torque about the μ_1 and μ_2 axes create very little mean torque about

174   the orthogonal axes ($\mu_{1\perp}$ and $\mu_{2\perp}$), even thoughout the magnitude of the oscillations through the

175   stroke is quite large (Fig. 6F).

176   Next, we constructed a set of systematically distorted stroke patterns ranging from steady

177   flight conditions to kinematics that generate peak torque about the μ_1, μ_2, and yaw axes, and then

178   replayed these on the robot (see Materials & Methods). For yaw, torque measured using the

179   robot matched the values derived from body motion (Eqn 1) throughout the entire range of

180   distorted kinematics (average difference ~2%, Fig. 7A). For the μ_1 and μ_2 axes, the torques

181   derived from body motion are about 66% and 59% (respectively) from that measured with

182   robofly, suggesting that the dynamic model for roll and pitch (Eqns 2-4) may be oversimplified

183   or that the torque measured using a robot in a fixed reference frame do not accurately model the

184   free flight case. We also measure the cross-talk (i.e. torque generated around orthogonal axes)

185   produced by the kinematics associated with production of peak torque around the different

186   torque axes. For the yaw case, the cross-talk about the roll and pitch axes was -24% and 27% of

187   $|T_{yaw}|$, respectively (Fig. 7A). For the μ_1 case, the cross-talk about the $\mu_{1\perp}$ and yaw axes was 3%

188   and 45% of $|T\mu_1|$, respectively, and for the μ_2 case, the cross-talk around the $\mu_{2\perp}$ and yaw axes

189   was 23% and 47% of $|T\mu_2|$, respectively (Fig. 7B). The cross-talk between the yaw torque and

190   torque about the axes in the stroke-plane (Fig. 7A,B) shows that our method did not enable us to

191   completely separate the effect of torque and force production about the different principal axes.

192   This is most likely due to the fact that during saccadic maneuvers, flies increase force production

193   and produce torque about the different axes in synchrony. So, wingbeats that produced large

194   torque about the axes in the stroke-plane tended to also produce high yaw torque and increased

195   aerodynamic forces (Figure 5).

196   Next, we varied the kinematics for each of the three wing angles in isolation to determine

197   their relative contribution to torque (Fig. 7C,D). As was also the case for evasive maneuvers

198   (Muijres et al., 2014), the sum of torques resulting from modulating the different components of

199   wing motion separately matches the torque generated by modulating all components

200   simultaneously, indicating a remarkable degree of linearity. For all torque axes, wing rotation

201   angle had the strongest effect on changes in total torque, whereas changes in stroke amplitude

202   and stroke deviation contribute modestly to the control of torque around the μ_1 and μ_2 axes and

203   make almost no contribution to the control of yaw torque (Fig. 7C,D).

204   As suggested by a previous study of *D. melanogaster*, a change in the mean offset of the

205   rotation angle will create yaw torque by increasing the angle of attack during one half-stroke and

206   decreasing it on the other (Bergou et al., 2010). However, another means by which wing rotation

207   might influence torque is through changes in the timing of wing rotation relative to stroke

208   reversal, which can change forces via unsteady mechanisms (Dickinson et al., 1999). To explore

209   the relative importance of these two potential mechanisms, we estimated both the relative phase

210   shift and mean offset of the time course of the wing kinematic angles for the left and right wings

211   during the strokes that generated peak torque (Figs 8, S3). Figure 8C-F shows that there is a

212   phase shift of ~5° in the wing rotation angle of the left wing relative to the right during wing

213   strokes that produce peak torque around the μ_1 and μ_2 axes, but there is no evidence for a change

214   in mean offset. In the case of yaw torque, a phase shift of ~3° is accompanied by an offset of ~4°.

215   Thus, although torque about the yaw, μ_1, and μ_2 axes are all primarily controlled by changes in

216   the time course of wing rotation, our results suggest that the relative mechanisms are different.

217   Flies regulate the torque about the μ_1 and μ_2 axes by modulating unsteady rotational lift

218   mechanisms during stroke reversal (Dickinson et al., 1999), whereas yaw torque is controlled by

219   a combination of unsteady effects at stroke reversal and differences in drag during the

220   translational phase of the two half strokes (Bergou et al., 2010). This interpretation is consistent

221   with the time history of the changes in torque throughout the wingbeat for the kinematics that

222   produce peak torques (Fig. 6). Yaw torque is produced mostly during the translation phase of the

223   wingbeat (Fig. 6D), which is indicative of an asymmetry in drag production between the two

224   wings. In contrast, changes in torque about the μ_1 and μ_2 axes (relative to a steady wing stroke)

225   occur mostly at the start of each wingstroke (Fig. 6E), suggesting modulations in rotational

226   effects.

227

DISCUSSION

229   Our analysis showed that fruit flies perform body saccades by executing stereotyped

230   banked turns (Fig. 2). The axes of the initial rotation (μ_1) and subsequent counter-rotation (μ_2)

231   are aligned 36° and 8° from the roll axis of the fly, respectively (Fig. 4B). Flies control the size of

232   the turn by regulating the magnitude of torque around these rotation axes (Fig. 4F), and not by

233   adjusting their orientation as they do during more rapid escape maneuvers (Muijres et al., 2014).

234   Flies also rotate unidirectionally around the yaw axis during saccades to correct for the

235   misalignment between body orientation and heading (i.e. sideslip) that accumulates as a result of

236   the banked turn.

237   Using a simple dynamic model, we were able to estimate the relative contribution of

238   inertia and damping during a saccade (Fig. 3). We found that yaw dynamics are dominated by

239   passive damping that results from the reciprocal flapping pattern, as suggested by Hesselberg &

240   Lehmann (2007). Pitch dynamics, in contrast, are dominated by inertia, and the contribution of

241   damping and inertia in roll dynamics is roughly equal. Thus, saccade dynamics are quite

242   complex and accurate models must include both inertial and damping terms (Bergou et al., 2010;

243   Cheng et al., 2010; Dickson et al., 2010; Fry et al., 2003; Hedrick et al., 2009; Hesselberg and

244   Lehmann, 2007). The model for rapid turns proposed by Hedrick and coworkers (2009) in which

245   insects rely primarily on passive damping to generate counter-torque may not be as general as

246   proposed, assuming that other insects also employ banked turns and do not simply rotate about

247   the yaw axis.

248   The maneuver that we have measured in fruit flies using high speed videography is

249   similar to the body saccades of blowflies, measured elegantly by Schilstra & Hateren (1999)

250   using tiny inductive coils. Thus, at least two species of flies, encompassing a rather large range

251 in scale, execute banks turns to produce rapid changes in flight direction. Given the high degree

252 of similarity within their nervous systems, it is likely that body saccades of *Drosophila* and

253 *Calliphora* are generated by homologous circuits.

254   Visually-elicited escape maneuvers (Muijres et al., 2014) and voluntary body saccades in

255 fruit flies both consist of a banked turn, but the dynamics of the two maneuvers are different

256 enough to suggest that they are produced by distinct motor programs. Although body saccades

257 are fast, the changes in heading during evasive maneuver are faster, consistent with a more

258 pronounced rotation of the body that reorients the mean force vector to produce a larger

259 horizontal component. As a consequence, flies do not maintain weight support during the initial

260 stages of an escape maneuver, whereas they do during body saccades (Fig. 2F,J). Similarly, yaw

261 is poorly controlled during the initial stages of an evasive maneuver, resulting in large sideslip

262 angles that are corrected long after the fly changes heading. During a body saccade, the yaw

263 correction is better coordinated with the banked turn, so that sideslip is minimized throughout the

264 maneuver. Perhaps the greatest difference between the two maneuvers relates to the manner by

265 which the magnitude of the change in heading is controlled. Flies regulate the turn angle of a

266 saccade by varying torque magnitude about two highly stereotypic axes (μ_1 and μ_2), whereas

267 during evasive maneuvers the turn angle is controlled by adjusting the direction of the body

268 rotation axis within the stroke plane. One interpretation that unifies all these differences is that

269 evasive maneuvers may be optimized to alter flight heading as quickly as possible at the expense

270 of flight control and motion blur, whereas body saccades are optimized to restrict retinal slip to a

271 brief period.

272   The transition from rotation to counter-rotation during a body saccade is quite fast and

273 such a pattern might be generated in a feed-forward manner by a central motor program or,

274   alternatively, the initial rotation might trigger the counter-rotation via a sensory-mediated reflex.

275   The halteres are a likely source of such feedback, as they mediate compensatory reactions to

276   imposed rotations (Dickinson, 1999; Nalbach, 1994; Ristroph et al., 2010; Sherman and

277   Dickinson, 2003). Previous studies of saccades using a magnetic tether in which the animal is

278   free to rotate about its yaw axis suggest that haltere feedback, but not visual feedback, plays a

279   role in terminating saccades (Bender and Dickinson, 2006b). Interpretation of these prior

280   experiments using magnetic tethers is complicated, however, by the new free flight data which

281   show that *Drosophila* bank to change direction at the start of the saccade. Given their time

282   course, the slow unidirectional saccade-like rotations that flies exhibit on magnetic tethers most

283   likely represent the slower yaw phase of a free flight saccade. Thus, the manipulation

284   experiments performed by Bender and Dickinson (Bender and Dickinson, 2006b) might indicate

285   that haltere feedback is involved in regulating the duration of the slower yaw correction phase of

286   a saccade but do not directly address the question of whether feedback triggers the faster

287   counter-rotation phase of the initial banked turn.

288   By exploiting the high throughput capabilities of our tracking system, we were able to

289   make accurate measurements of the changes in wing motion during saccades (Fig. 6). All three

290   wing angles (ϕ, γ, α) exhibit a biphasic modulation during the time course of the saccade, as

291   expected from the production of torque and counter-torque (Fig. 5B-G). These data are

292   consistent with the previous observations of Fry and coworkers (Fry et al., 2003), although these

293   authors misinterpreted this biphasic pattern as indicating active breaking around the yaw axis,

294   when it is more likely that they observed evidence for the counter-rotation about the μ_2 axis.

295   Replaying the pattern of wing motion on a stationary robot generated a time history of forces and

296   moments that matched those derived from free flight body dynamics reasonably well, but not

297   perfectly (Fig. 5H-K). The match for total flight force and yaw were quite good, whereas roll

298   torque based on the wing kinematics and the robot measurements were larger than roll torque

299   derived from body dynamics. This mismatch is perhaps not too surprising, given that the saccade

300   basically consists of a rapid roll and counter-roll (i.e. the μ_1 and μ_2 axes are not too far off the

301   roll axis). Thus, errors that derive from the fact that the kinematics from a rotating fly were

302   replayed on a stationary robot would be particularly large for this degree of freedom. Other

303   sources of error include the possible inaccuracies of our dynamics model, which did not include

304   cross terms and used damping coefficients based on steady-state approximations.

305   By mining the entire database, we were able to determine the pattern of wing motion that

306   correlated with peak torque production around the μ_1, μ_2, and yaw axes (Fig. 6), and then to

307   determine the relative contribution of the three wing angles to the moments by playing

308   systematically distorted wing patterns through the robotic fly (Fig. 7). The results indicate that

309   changes in the time history of the wing rotation angle, which strongly influences the angle-of-

310   attack, are by far the most important for regulating torque about the μ_1, μ_2, and yaw axes (Fig.

311   7C,D). However, the torque modulations about the yaw axis and about the two axes in the stroke

312   plane (μ_1 and μ_2) appear to occur via two distinct aerodynamic mechanisms (Fig. 8). As

313   suggested by Bergou and coworkers (2010), changes in the mean offset of the wing rotation

314   angle magnitude lowers the angle-of-attack during one half stroke while raising it on the other,

315   thus producing an upstroke-to-downstroke imbalance in drag and thus net torque around the axis

316   normal to the stroke plane. Although our results support this mechanism (Fig. 6A,D and Fig.

317   7A,B), we also found that the flies adjust the relative phase of wing rotation as well, thus

318   creating additional yaw torque via unsteady mechanisms at stroke reversal (Dickinson et al.,

319   1999; Sane and Dickinson, 2002). Flies also create torque about the μ_1 and μ_2 axes via changes

320   in wing rotation angle, but in these cases the effect appears to be mediated almost entirely by

321   changes in phase, and thus through unsteady effects at stroke reversal (Fig. 6E and Fig. 7C-F).

322   One possible explanation for this difference is that changes in angle of attack during the

323   translational portion of the stroke would be undesirable for regulating roll because they would

324   generate large cross-talk in yaw torque.

325   A quite surprising result of our analysis was the relatively small importance of stroke

326   amplitude and stroke deviation in the control of torque during saccades (Fig. 7C,D). This was

327   particularly true for yaw torque, an observation that complicates interpretation of many tethered

328   flight studies, which collectively show that flies generate large changes in stroke amplitude in

329   response to both visual and mechanosensory rotations about the yaw axis (e.g. Sherman &

330   Dickinson 2003), as well as transient spontaneous changes that have been ubiquitously

331   interpreted as fictive saccades. These changes in stroke amplitude were quite large and clearly

332   correlated with yaw torque (Tammero, 2004). Why do tethered flies generate such large changes

333   in stroke amplitude that do not seem necessary to generate yaw torque in free flight? One

334   possibility is that the stroke amplitude signal measured during fictive saccades is indicative of

335   the roll and pitch required for a banking maneuver, and not for yaw production *per se*. If true,

336   this has immediate implications for the underlying circuitry as it is noteworthy that the stroke

337   amplitude changes associated with fictive saccades are unidirectional, i.e. there is no evidence of

338   an attempt at a programmed counter-rotation.

339   Recently, Schnell and coworkers (Schnell et al., 2014) suggested that the basic optomotor

340   circuit in *Drosophila* includes an integral feedback term that might be mediated by Ca^{2+}

341   dynamics in the terminals of the interneurons that encode horizontal rotation. Because the

342   putative integrator winds up with prolonged stimulation, flies generate extremely large motor

343 responses during typical open-loop optomotor experiments. Although this hypothesis explains

344 why the optomotor responses in tethered flight are so large relative to the kinematics changes

345 exhibited during free flight maneuvers, it does not explain why flies generate such enormous

346 changes in stroke amplitude when presented with stimuli that should elicit the production of yaw

347 torque. Perhaps flies respond to visual rotation about the yaw axis by producing not just yaw

348 torque but also roll torque, because they are attempting to turn via banking, as has been

349 suggested by previous authors (Mronz and Lehmann, 2008). This hypothesis could be tested in

350 the future by measuring free flight responses to horizontal motion.

351

352 **MATERIALS AND METHODS**

353 *Animals and experimental setup*

354 The methods used in this study were identical to those described in detail elsewhere

355 (Muijres et al., 2014) and are only briefly outlined here. Experiments were performed on 1-to-5

356 day old male and female *Drosophila hydei*, from a laboratory stock reared in a 14:10 (L:D) light

357 cycle. Each day, approximately 50 one-day-old flies were released in the experimental chamber

358 4 hours before their subjective dawn, after which experiments ran for 8 hours. The experimental

359 chamber consisted of a transparent cylindrical enclosure, surrounded by a panoramic array of

360 green LED panels (Reiser and Dickinson, 2008) that provided a uniform illumination of 70 lux.

361 Flies were filmed using three synchronized high-speed cameras (Photron SA5 with AF Nikor

362 60mm lenses, lens aperture = f/22), which viewed the central portion of the arena from above and

363 from two orthogonal side positions (Fig. 1A). The cameras operated at 7,500 frames per second

364 with an image resolution of 1024x1000 pixels, exposure time of 1/30,000 second, and image

365 depth of 12 bits. Due to limitations in optics, the region of interest was restricted to a cube ~40

366 mm on each side. Each camera view was backlit using high intensity infrared light panels, which

367 were strobed in synchrony with every exposure. To maintain the inside temperature at ~25°C, we

368 passed refrigerated air around the outside of the flight chamber. At the start and end of each 5-

369 day recording period, we calibrated the camera system using direct linear transformation (DLT)

370 (Christoph Reinschmidt; http://isbweb.org/software/movanal.html).

371 Throughout each experimental session, the cameras sampled continuously. When a fly

372 flew directly through the center of the region of interest, it tripped an infrared laser crossbeam,

373 which automatically triggered the storage of 372 ms of data both before and after the trigger

374 event. We captured more than 300 flight sequences, of which the majority consisted of a straight

375 flight path, but occasionally a fly would perform a saccadic maneuver (Supplementary Movie

376 S1). Although fruit flies are largely insensitive to infrared light, we were concerned that the high

377 intensity of the IR trigger lasers might elicit behavioral responses. For this reason, we only

378 analyzed the saccades that flies initiated before passing through the trigger point. Given our

379 sampling methods, we have no way of knowing whether any given saccade was elicited by visual

380 expansion or via some internal stochastic event.

381

382 *Measuring body and wingbeat kinematics*

383 We manually selected 44 sequences from the entire data set for detailed analysis, which

384 we subjectively classified as body saccades based on visual inspection of the raw video

385 sequences. To extract kinematics throughout these saccades, we used an automatic machine-

386 vision system as described in a recent analysis of escape maneuvers (Fig. 1B) (Muijres et al.,

387 2014). The tracking routine provided us with Kalman filtered estimates of the body and wing

388 kinematics throughout each flight sequence (Fig. 1C, Supplementary Movie S2) (Muijres et al.,

389 2014).

390   For all Kalman filters, the cross-product values in the error covariance matrices (R and

391   Q) were set to zero, and covariance matrix R was set to identity. Thus, adjusting the parameters

392   in covariance matrix Q controlled Kalman smoothing. For positional data, we used a linear

393   Kalman filter and the smoothing parameters of matrix Q were scaled according to a Taylor

394   series. Q values corresponding to position were set to dt^2, velocity values were set to 1, and

395   acceleration values were set to $1/dt^2$, where dt is the time step between two measurements

396   (inverse of the frame rate).

397   To filter body and wing orientation data, we used an extended Kalman filter with two

398   filtering steps (Yun & Bachmann, 2006), because quaternion update is non-linear. For body

399   orientation filtering, we used the following Q parameters. For the first iteration, Q parameters

400   associated with angular velocities and angular accelerations were set to zero, and parameters

401   associated with quaternions were set to 0.003. For the second iteration, angular velocity

402   parameters were set to 0.0001, angular acceleration parameters were set to $0.0001/dt^2$, and

403   quaternion parameters were set to 1. For wing orientation filtering, we used a similar strategy but

404   less smoothing was desired. For the first iteration, angular velocity parameters and angular

405   acceleration parameters were set to zero, and quaternion parameters in Q were set to 1. For the

406   second iteration, angular velocity parameters in Q were set to $1/dt^2$, angular acceleration

407   parameters were set to 0, and quaternion parameters were set to 1.

408   Body position data consists thus of Kalman filtered estimates of position, $X(t)$, velocity,

409    $U(t)$, and linear acceleration, $a(t)$. Based on $U(t)$ and $a(t)$, we determined the start and end of

410   each saccade by estimating horizontal accelerations normal and tangential to the flight path ($a_N(t)$

411   and $a_T(t)$, respectively). Using an expectation maximization-based clustering analysis on $a_N(t)$

412   and $a_T(t)$ for all measured flight sequences (Muijres et al., 2014), we divided flight sequences

413   into steady and maneuvering segments, such that steady segments satisfied $a_N < 0.19g$ and -

414    $0.17g < a_T < 0.14g$, where g is gravitational acceleration. The times at which a saccade starts (t_{start})

415   and ends (t_{end}) were defined as the moments when body accelerations passed these threshold

416   values. Note that these points in time do not encompass the entire length of the maneuver, but the

417   method enabled us to systematically and objectively define and align the saccades.

418   Based on the velocity data, we determined flight heading, $\sigma(t)$, which we used to

419   determine the turn angle, $\Delta\sigma$, for each saccade. $U(t)$ was also used to determine changes in flight

420   speed, $dU(t)$, throughout the maneuver relative to the start of each sequence. Linear acceleration,

421    $a(t)$, was used to estimate the direction, σ_a, and magnitude, a_{hor}/g, of normalized acceleration

422   within the horizontal plane, as well as the magnitude of the vertical acceleration, a_z/g. Body

423   orientation was expressed in the body Euler angles (yaw, ψ_E; pitch, θ_E; and roll, η_E) in the world

424   reference frame and normalized angular velocity of the body, $\boldsymbol{\Omega} = \{\omega_x, \omega_y, \omega_z\}$, in the body

425   reference frame (Fig. 1C). All rotation rates were normalized using f_{steady}, where f_{steady} is the

426   wingbeat frequency during steady flight for *D. hydei*, (~ 189 Hz, from Muijres et al. 2014).

427   Each tracked wingbeat was expressed by the wingbeat frequency, f, and three Euler

428   angles within the body reference frame: wing stroke angle, ϕ, stroke deviation angle, γ, and wing

429   rotation angle, α (Fig. 1C). Note that all body and wing orientation variables are defined relative

430   to the stroke plane, which is defined as horizontal during steady flight (Fig. 1C). For *D. hydei*,

431   this is at an inclination angle of 47.5° relative to the long axis of the body (Muijres et al., 2014).

432

433   ***Estimating aerodynamic forces and torques based on body dynamics***

434   The aerodynamic forces throughout a flight maneuver can be estimated directly from

435   body accelerations as:

436

437    $F(t) = (a(t)+g)/|g|,$ (1)

438

439   where F is the aerodynamic force vector normalized with body weight, mg, and $g = \{0, 0, g\}$ is

440   the gravitational acceleration vector. The orientation of this force vector in the body frame was

441   defined as the roll (ξ) and pitch (β) angle of F relative to the stroke-plane normal (Fig. 1C), and

442   is calculated based on the body Euler angles and F.

443   The aerodynamic torque produced throughout a maneuver was estimated from the body

444   rotations. Because aerodynamic damping has been shown to be an important source of passive

445   stability in flapping flight (Hesselberg and Lehmann, 2007; Hedrick et al. 2009), we estimate

446   normalized torque T using a linear model based on both normalized angular velocities and

447   accelerations:

448

449    $T(t) = C\,\boldsymbol{\Omega}(t) + I\,\dot{\boldsymbol{\Omega}}(t),$ (2)

450

451   where $\dot{\boldsymbol{\Omega}}$ is the angular acceleration vector of the body normalized by f^2_{steady}, and which is

452   estimated by numerically differentiating $\boldsymbol{\Omega}$. C is the aerodynamic damping coefficient matrix

453   normalized by mgl/f_{steady}, where l is wing length, and I is the body inertia matrix normalized by

454   mgl/f^2_{steady}. Because aerodynamic torque produced by a wing scales with the product of force and

455   wing length, we normalized torque by $|a+g|ml$. We modeled C as

456

457    $C = \begin{bmatrix} C_{roll} & 0 & 0 \\ 0 & C_{pitch} & 0 \\ 0 & 0 & C_{yaw} \end{bmatrix},$ (3)

458

459   and I as

460

461
$$I = \begin{bmatrix} I_{roll} & 0 & 0 \\ 0 & I_{pitch} & 0 \\ 0 & 0 & I_{yaw} \end{bmatrix}.$$
(4)

462

463   Thus, our simplified model assumes that all interaction coefficients in both C and I are

464   negligible.

465   The damping coefficients in C were based on damping estimates for *D. melanogaster*

466   reported in literature (Cheng et al., 2009; Dickson et al., 2010). The yaw-damping coefficient for

467   *D. hydei* (C_{yaw}) was estimated by scaling values measured for *D. melanogaster* using a robotic

468   model (Dickson et al., 2010). Roll and pitch damping for *D. hydei* were based on computational

469   estimates of damping coefficients in *D. melanogaster* (Cheng et al., 2009). For consistency

470   among the damping coefficients for the three degrees-of-freedom, we first linearly scaled all

471   damping coefficients estimated for *D. melanogaster* by Cheng et al. (2009) equally, such that

472   yaw damping was equal to that reported by Dickson et al. (2010), and then scaled these values to

473   the slightly larger species, *D. hydei*. This resulted in the following normalized roll, pitch, and

474   yaw damping coefficients: $C_{roll} = 0.22$; $C_{pitch} = 0.08$; $C_{yaw} = 0.41$. Note that the damping

475   coefficient for yaw is 5 times greater than for pitch and twice as large as that for roll.

476   Inertia coefficients within the stroke-plane reference frame were estimated based on a

477   cylindrical body model with body mass m and pitch angle of 47.5° and a wing model consisting

478   of a horizontal disk divided into 100 concentric rings (Fig. 1C). Each ring has a homogenously

479   distributed mass equal to the mass of the local spanwise wing section plus its added fluid mass.

480   Following (Ellington, 1984), total wing mass was estimated as 5% of body mass, and added mass

481   was equal to a cylindrical fluid mass circumventing each wing section. This resulted in

482   normalized roll inertia $I_{roll} = 0.64$, normalized pitch inertia $I_{pitch} = 1.07$, and normalized yaw

483   inertia $I_{yaw} = 0.57$.

484

485   ***Correlating wingbeat kinematics with torque production***

486   To determine how a fly controls torque throughout a saccade, we correlated changes in

487   wing kinematics with torques estimated from body dynamics (Eqn 2). Wing kinematics were

488   correlated with torque about an axis defined by a torque vector, ***T'***, by parsing the complete

489   dataset into steady wingbeats and wingbeats in which the fly generated some absolute magnitude

490   of ***T'*** (|***T'***|) that was larger than one standard deviation of the entire distribution of |***T'***| for all

491   wingbeats in the dataset. Changes in kinematics angles throughout a wingbeat relative to the

492   steady wingbeat angles were linearly correlated with the stroke-averaged normalized torque

493   estimated from body dynamics (Eqn 2) as:

494

495    $mod(\kappa, \boldsymbol{T'})_i = (\kappa_i - \kappa_{steady}) / |\boldsymbol{T'}|_i,$ (5)

496

497   where $mod(\kappa, \boldsymbol{T'})_i$ is the wingbeat modification variable for kinematic angle κ (representing

498   either ϕ, γ, or α) of the ith wingbeat in the dataset of |***T'***| producing wingbeats. κ_{steady} is the

499   equivalent kinematics angle distribution of the average steady wingbeat of *D. hydei*, based on

500   1603 wingbeats measured by Muijres et al. (2014) (Fig. 1D).

501   Variation in wingbeat frequency (which is equal for both wings) is excluded from this

502   analysis because such modulation could not alter torque directly. By fitting a Fourier series

503   through the complete dataset of $mod(\kappa, \boldsymbol{T'})$, we determined the average wing kinematics

504   modulation distributions, $MOD(\kappa, \boldsymbol{T'})$ for each kinematics angle and torque axis. Fourier series

505   were fitted using a Levenberg-Marquardt algorithm and are defined as:

506

507    $$k(t^*) = a_0 + \sum_{n=1}^{N} a_n \cos(2\pi n t^*) + b_n \sin(2\pi n t^*),$$ (6)

508

509   where a_n and b_n are the Fourier series coefficients for the nth order, and τ is normalized time for

510   each wingbeat ($t^* = t\,f$). All Fourier series ($MOD(\phi, \boldsymbol{T'})$, $MOD(\gamma, \boldsymbol{T'})$, $MOD(\alpha, \boldsymbol{T'})$) were 8th order

511   ($N=8$). From the $MOD(\kappa, \boldsymbol{T'})$ estimates, the set of wing kinematics variables that would result in a

512   given amount of torque $|\boldsymbol{T'}|$ about torque axis $\boldsymbol{T'}$ can be reconstructed by:

513

514    $$\kappa = \kappa_{\text{steady}} + |\boldsymbol{T'}|\, MOD(\kappa, \boldsymbol{T'}).$$ (7)

515

516   ***Measuring aerodynamic forces and torques using a dynamically scaled robot***

517   Apart from estimating aerodynamic forces and torques from body dynamics (Eqn 1 and Eqn 2,

518   respectively), we also estimated forces and torques from wing kinematics, using a dynamically

519   scaled robot in a fixed body reference frame (Dickinson et al., 1999). This technique enabled us

520   to study the aerodynamics of saccadic maneuvers in a systematic and detailed manner. We

521   replayed the wingbeat kinematics in a fixed body reference frame because aerodynamic and

522   inertial effects of body rotations were modeled using Eqn 2. Note that aerodynamics effects due

523   to body translations were ignored.

524   To assess the accuracy of our methods, we compared torque measurements based on the

525   wingbeat kinematics with the torque estimates based on body dynamics (Eqn 2). This analysis

526   was performed on two sets of data. The first dataset consisted of the mean wing kinematics and

527   body dynamics throughout the average saccade, estimated by aligning the wingbeats from all

528   maneuvers. This enabled us to test qualitatively whether the measured changes in wingbeat

529   kinematics captured the forces and torques produced throughout the saccade. The second dataset

530   was based on the systematic analysis described above, in which we correlated wingbeat

531   kinematics with torque production. Using Eqn 7, we constructed a set of kinematics patterns that

532   should produce a systematically increasing amount of body torque about a specific body axis $\boldsymbol{T}$".

533   The range of body torques was chosen such that it captured the complete behavioral envelope of

534   measured torque production. We defined a body torque distribution spanning a range from zero

535   body torque (steady flight) to a torque equal to approximately three times the standard deviation

536   of the $|\boldsymbol{T}"|$ distribution for all measured wingbeats, and parsed it into 8 values. For each, we

537   created the matching deformed wingbeat kinematics using Eqn 7. We then replayed the set of

538   systematically distorted wing kinematics on the robotic fly and measured the resulting stroke-

539   averaged forces and torques about all three orthogonal body axes, and compared these values

540   with the values of body torques. This approach also enabled us to determine cross-talk between

541   torque modulations about the different orthogonal axes. The distributions of $|\boldsymbol{T}"|$ and the

542   corresponding wing kinematics constructed using Eqn 7 were also used to study the effects of

543   stroke, deviation, and wing rotation angle on torque production. Using a method similar to that

544   described by Muijres et al. (2014), we systematically modulated one wing kinematics variable,

545   while maintaining steady kinematics for the other angles, and replayed these on the robot.

546   Cases in which body torque was equal to three standard deviations of the $|\boldsymbol{T}"|$ distribution,

547   which we considered as an estimate for peak torque production, were analyzed in more detail

548   using two complementary methods. First, we replayed the wingbeat kinematics that

549   corresponded to this peak torque (estimated using Eqn 7) on the robot and measured force and

550   torque throughout the wingbeat. Second, we analyzed the changes in wing kinematics that result

551   in peak torque production. For each kinematic angle, the difference in kinematics between the

552   left and right wing might result from temporal phase shift, from a shift in the mean value, or

553   from higher order modulations in the time history (Fig. 1D). For each kinematic variable, we

554   estimated the temporal phase shift and offset in mean value between the left and right wing by

555   systematically translating the left wing data along the time (τ) and ordinate (κ) axes. For each

556   combination of $\Delta\tau$ and $\Delta\kappa$, we determined the root mean square error (RMSE) between the right

557   wing and shifted left wing values. The combination of $\Delta\tau$ and $\Delta\kappa$ at which RMSE was minimum

558   defines the phase shift an angular offset between left and right wing for that wing kinematics

559   angle and $|\boldsymbol{T}"|$ axis combination. The corresponding magnitude of RMSE quantifies how well the

560   wing kinematics modulations are described by $\Delta\tau$ and $\Delta\kappa$, relative to any higher order

561   modulations.

562   **List of symbols and abbreviations**

A	Amplitude
$\boldsymbol{a} = \{a_x, a_y, a_z\}$	Acceleration vector in the world reference frame
a_N	Horizontal acceleration normal to the flight path
a_T	Horizontal acceleration tangential to the flight path
a_n	Fourier series coefficient
b_n	Fourier series coefficient
dt	Time step between measurements (inverse of camera frame rate)
$\boldsymbol{C}$	Normalized aerodynamic damping coefficient matrix

dU	Flight speed relative to the start of the maneuver
$\boldsymbol{F}$	Normalized aerodynamic force vector in the world reference frame
f	Wingbeat frequency
$\boldsymbol{g} = \{0,0,g\}$	Gravitational acceleration vector
g	Gravitational acceleration scalar
$\boldsymbol{I}$	Normalized inertia coefficient matrix
l	Wing length
m	Body mass
mg	Body weight
$\boldsymbol{Q}$	Error covariance matrix of Kalman filter
$\boldsymbol{R}$	Error covariance matrix of Kalman filter
$\boldsymbol{T}$	Normalized aerodynamic torque vector in the body reference frame
$\boldsymbol{T'}$	An arbitrarily defined aerodynamic torque vector
t	Time relative to the start of the saccade
t^*	Normalized time within a wingbeat relative to the start of the downstroke
$\boldsymbol{U} = \{u,v,w\}$	Velocity vector in the world reference frame
$\boldsymbol{X} = \{x,y,z\}$	Position vector in the world reference frame
$\boldsymbol{X_B} = \{x_B,y_B,z_B\}$	Position vector in the body reference frame
α	Rotation angle of the wing around its long axis
β	Pitch angle of the aerodynamic force vector in the body reference frame
γ	Deviation angle of the wing out of the stroke plane
$\Delta\alpha$	Shift of the mean wing rotation angle of the left wing relative to the right
$\Delta\tau$	Phase shift of the left wing movement relative to the right wing movement
$\Delta\kappa$	Shift of the mean wing kinematic angle of the left wing relative to the right
$\Delta\sigma$	Turn angle of the saccade
Δt	Duration of a saccadic turn
η	Body roll angle derived from roll rate ω_x
η_E	Body roll Euler angle in the world reference frame
θ	Body pitch angle derived from pitch rate ω_y

θ_E	Body pitch Euler angle in the world reference frame
κ	Wing kinematics angles
μ	Torque axis angle within the stroke plane relative to the roll torque axis
μ_1	Primary torque axis angle (mean torque angle during the initial phase of the banked turn)
$\mu_{1\perp}$	Angle within the stroke plane and orthogonal to μ_1
μ_2	Counter-torque axis angle (mean torque angle during the counter-torque phase of the banked turn)
$\mu_{2\perp}$	Angle within the stroke plane and orthogonal to μ_2
ξ	Roll angle of the aerodynamic force vector in the body reference frame
σ	Heading (the direction of the horizontal body velocity component)
σ_a	Direction of horizontal body acceleration component
τ	Phase within a wingbeat relative to the start of the downstroke
ϕ	Stroke angle of the wing within the stroke plane
ψ	Body yaw angle derived from yaw rate ω_z
ψ_E	Body yaw Euler angle in the world reference frame
$\mathbf{\Omega} = \{\omega_x, \omega_y, \omega_z\}$	Normalized rotation rate vector of the body in the body reference frame
ω_x	Normalized body roll rate in the body reference frame
ω_y	Normalized body pitch rate in the body reference frame
ω_z	Normalized body yaw rate in the body reference frame

563

567

Competing interests

The authors declare no competing financial interests.

570

571 **Author contributions**

572 F.T.M and M.H.D planned experiments and wrote the paper. F.T.M. and N.A.I. collected data in

573 flight arena, ran the automated machine vision tracking software, and identified sequences with

574 saccadic turns. M.J.E. collected data using the robotic fly. F.T.M. analyzed the data, with the

575 help of M.J.E. and M.H.D.

576

582

583 **References**

584 **Bender, J. A. and Dickinson, M. H.** (2006a). Visual stimulation of saccades in magnetically tethered Drosophila. *J.*
585   *Exp. Biol.* **209**, 3170–82.

586 **Bender, J. A. and Dickinson, M. H.** (2006b). A comparison of visual and haltere-mediated feedback in the control
587   of body saccades in Drosophila melanogaster. *J. Exp. Biol.* **209**, 4597–606.

588 **Bergou, A. J., Ristroph, L., Guckenheimer, J., Cohen, I. and Wang, Z. J.** (2010). Fruit Flies Modulate Passive
589   Wing Pitching to Generate In-Flight Turns. *Phys. Rev. Lett.* **104**, 148101.

590 **Censi, A., Straw, A. D., Sayaman, R. W., Murray, R. M. and Dickinson, M. H.** (2013). Discriminating external
591   and internal causes for heading changes in freely flying Drosophila. *PLoS Comput. Biol.* **9**, e1002891.

592 **Cheng, B., Fry, S. N., Huang, Q., Dickson, W. B., Dickinson, M. H. and Deng, X.** (2009). Turning dynamics and
593   passive damping in flapping flight. *2009 IEEE Int. Conf. Robot. Autom.* 1889–1896.

594 **Cheng, B., Fry, S. N., Huang, Q. and Deng, X.** (2010). Aerodynamic damping during rapid flight maneuvers in the
595   fruit fly Drosophila. *J. Exp. Biol.* **213**, 602–12.

596 **Collett, T. and Land, M.** (1975). Visual control of flight behavior in hoverfly, Syritta pipiens. *J. Comp. Physiol.*
597   **99**, 1–66.

598 **David, C.** (1978). The relationship between body angle and flight speed in free-flying Drosophila. *Physiol. Entomol.*
599   **3**, 191–195.

600 **Dickinson, M. H.** (1999). Haltere-mediated equilibrium reflexes of the fruit fly, Drosophila melanogaster. *Philos.*
601   *Trans. R. Soc. Lond. B. Biol. Sci.* **354**, 903–16.

602 **Dickinson, M. H.** (2014). Death Valley, Drosophila, and the Devonian toolkit. *Annu. Rev. Entomol.* **59**, 51–72.

603 **Dickinson, M. H., Lehmann, F.-O. and Sane, S. P.** (1999). Wing rotation and the aerodynamic basis of insect
604   flight. *Science (80-.).* **284**, 1954–1960.

605 **Dickson, W. B., Polidoro, P., Tanner, M. M. and Dickinson, M. H.** (2010). A linear systems analysis of the yaw
606   dynamics of a dynamically scaled insect model. *J. Exp. Biol.* **213**, 3047–61.

607 **Ellington, C. P.** (1984). The aerodynamics of hovering insect flight. I. The quasi-steady analysis. *Philos. Trans. R.*
608   *Soc. Lond. B. Biol. Sci.* **305**, 1–15.

609 **Elzinga, M. J., van Breugel, F. and Dickinson, M. H.** (2014). Strategies for the stabilization of longitudinal
610   forward flapping flight revealed using a dynamically-scaled robotic fly. *Bioinspir. Biomim.* **9**, 025001.

611 **Fry, S. N., Sayaman, R. and Dickinson, M. H.** (2003). The aerodynamics of free-flight maneuvers in Drosophila.
612   *Science* **300**, 495–8.

613 **Götz, K. and Wandel** (1984). Optomotor control of the force of flight in Drosophila and Musca. *Biol. Cybern.*

614 **Hateren, J. and Schilstra, C.** (1999). Blowfly flight and optic flow. II. Head movements during flight. *J. Exp. Biol.*
615   **1500**, 1491–1500.

616 **Hedrick, T. L., Cheng, B. and Deng, X.** (2009). Wingbeat time and the scaling of passive rotational damping in
617   flapping flight. *Science (80-.).* **324**, 252–255.

618 **Hesselberg, T. and Lehmann, F.-O.** (2007). Turning behaviour depends on frictional damping in the fruit fly
619   Drosophila. *J. Exp. Biol.* **210**, 4319–34.

620 **Land, M. F.** (1999). Motion and vision: why animals move their eyes. *J. Comp. Physiol. A.* **185**, 341–52.

621 **Maye, A., Hsieh, C.-H., Sugihara, G. and Brembs, B.** (2007). Order in spontaneous behavior. *PLoS One* **2**, e443.

622 **Mronz, M. and Lehmann, F.-O.** (2008). The free-flight response of Drosophila to motion of the visual
623   environment. *J. Exp. Biol.* **211**, 2026–45.

624 **Muijres, F. T., Elzinga, M. J., Melis, J. M. and Dickinson, M. H.** (2014). Flies Evade Looming Targets by
625   Executing Rapid Visually Directed Banked Turns. *Science (80-.).* **344**, 172–177.

626 **Nalbach, G.** (1994). The halteres of the blowfly Calliphora lI. Three-dimensional organization of compensatory
627   reactions to real and simulated rotations. *J. Comp. Physiol. A* 695–708.

628 **Reiser, M. B. and Dickinson, M. H.** (2008). A modular display system for insect behavioral neuroscience. *J.*
629   *Neurosci. Methods* **167**, 127–39.

630 **Reiser, M. B. and Dickinson, M. H.** (2013). Visual motion speed determines a behavioral switch from forward
631   flight to expansion avoidance in Drosophila. *J. Exp. Biol.* **216**, 719–32.

632 **Reynolds, A. M. and Frye, M. a** (2007). Free-flight odor tracking in Drosophila is consistent with an optimal
633   intermittent scale-free search. *PLoS One* **2**, e354.

634 **Ristroph, L., Bergou, A. J., Ristroph, G., Coumes, K., Berman, G. J., Guckenheimer, J., Wang, Z. J. and**
635   **Cohen, I.** (2010). Discovering the flight autostabilizer of fruit flies by inducing aerial stumbles. *Proc. Natl.*
636   *Acad. Sci.* **107**, 4820–4.

637 **Sane, S. P. and Dickinson, M. H.** (2002). The aerodynamic effects of wing rotation and a revised quasi-steady
638   model of flapping flight. *J. Exp. Biol.* **205**, 1087–1096.

639 **Schilstra, C. and Hateren, J.** (1999). Blowfly flight and optic flow. I. Thorax kinematics and flight dynamics. *J.*
640   *Exp. Biol.* **1490**, 1481–1490.

641 **Schnell, B., Weir, P. T., Roth, E., Fairhall, A. L. and Dickinson, M. H.** (2014). Cellular mechanisms for integral
642   feedback in visually guided behavior. *Proc. Natl. Acad. Sci. U. S. A.* **111**, 5700–5.

643 **Sherman, A. and Dickinson, M. H.** (2003). A comparison of visual and haltere-mediated equilibrium reflexes in
644   the fruit fly Drosophila melanogaster. *J. Exp. Biol.* **206**, 295–302.

645 **Stewart, F. J., Baker, D. a and Webb, B.** (2010). A model of visual-olfactory integration for odour localisation in
646   free-flying fruit flies. *J. Exp. Biol.* **213**, 1886–900.

647 **Tammero, L. F.** (2004). Spatial organization of visuomotor reflexes in Drosophila. *J. Exp. Biol.* **207**, 113–122.

648 **Tammero, L. F. and Dickinson, M. H.** (2002). The influence of visual landscape on the free flight behavior of the
649   fruit fly Drosophila melanogaster. *J. Exp. Biol.* **205**, 327–43.

650 **Van Breugel, F. and Dickinson, M. H.** (2014). Plume-tracking behavior of flying Drosophila emerges from a set of
651   distinct sensory-motor reflexes. *Curr. Biol.* **24**, 274–86.

652 **Van Breugel, F., Dickinson, M. H. and Breugel, F. Van** (2012). The visual control of landing and obstacle
653   avoidance in the fruit fly Drosophila melanogaster. *J. Exp. Biol.* **215**, 1783–98.

654 **Wagner, H.** (1986). Flight Performance and Visual Control of Flight of the Free-Flying Housefly (Musca
655   Domestica L.) III. Interactions Between Angular Movement Induced by Wide- and Smallfield Stimuli. *Philos.*
656   *Trans. R. Soc. B Biol. Sci.* **312**, 581–595.

657 **Wehrhahn, C., Poggio, T. and Bülthoff, H.** (1982). Tracking and chasing in houseflies (Musca). *Biol. Cybern.*
658   **130**, 123–130.

659 **Yun, X. and Bachmann, E. R.** (2006). Design, Implementation, and Experimental Results of a Quaternion-Based
660   Kalman Filter for Human Body Motion Tracking. *IEEE Trans. Robot.* **22**, 1216–1227.

661

662   **Figure Legends**

663 **Figure 1:** Experimental setup, coordinate system conventions, and flight tracks of saccades. (A)

664 The experimental setup consists of a cylindrical enclosure, three synchronized high-speed

665 cameras with IR LED backlighting, and a laser triggering system. (B) An automated machine

666 vision system tracks kinematics by projecting body and wing models onto the three orthogonal

667 camera images. (C) Measured parameters in the body reference frame. Body dynamics are

668 described by the angular velocity vector of the body, $\boldsymbol{\Omega} = \{\omega_x, \omega_y, \omega_z\}$ and its derivatives, about

669   the principal body axes $X_B = \{x_B, y_B, z_B\}$. Wing kinematics are defined by stroke angle within the

670   stroke plane, ϕ, deviation angle out of the stroke plane, γ, and wing rotation angle, α. Based on

671   the vector sum of body acceleration and the gravitational acceleration vector, we determined

672   normalized force vector, $\boldsymbol{F}$, with orientation in the body reference frame defined as force pitch

673   angle, β, and roll angle, ξ. (D) Temporal dynamics of the wing kinematics angles for a single

674   wingbeat. The black trace shows the average steady wingbeat of *D. hydei* that is used as a

675   baseline for our analysis (from Muijres et al., 2014). Grey traces show hypothetical wing angles:

676   stroke angle has a phase shift of $\Delta\tau = 5°$ relative to the steady wingbeat, wing deviation has a

677   mean deviation angle shift of $\Delta\gamma = 5°$, and wing rotation angle has both a shift of $\Delta\tau = 5°$ and $\Delta\alpha$

678    $= 5°$. (E,F) Side view (E) and top view (F) of the flight tracks of all 44 trials. Traces are color-

679   coded with time according to the scale bar in (E). Note that all left-handed turns have been

680   mirrored into right-handed turns, and all sequences were aligned according to position and

681   heading at the start of the saccadic maneuver ($t_{start} = 0$ ms).

682

683   **Figure 2:** Saccades in flies consist of banked turns. (A) Heading and speed (depicted as vectors

684   of horizontal velocity component) after the saccades for all measured trials separately (grey) and

685   its mean (black solid vector), relative to the aligned initial zero heading (black dotted mean

686   velocity vector). Speed is scaled according to the reference vector of 0.1 m/s. (B-L) temporal

687   dynamics of experimental parameters. (B) Heading relative to initial heading of $0°$, σ. (C)

688   Changes in flight speed relative to initial flight speed, dU, (D) Direction of the horizontal

689   component of body acceleration in the world reference frame, σ_a. (E) Horizontal component of

690   normalized body acceleration, a_{hor}/g. (F) Vertical component of normalized body acceleration,

691   a_z/g (negative values are shown such that upwards accelerations are in the positive y axis

31

692   direction). (G-I) Normalized roll rate (G), pitch rate (H), and yaw rate (I). (J) $|\boldsymbol{F}|$, normalized

693   aerodynamic force generated by the fruit fly. (K,L) ξ, roll angle (K), and β, pitch angle (L) of $\boldsymbol{F}$

694   (see also Fig. 1C). In B-L, grey traces depict data from separate trials and the black traces with

695   grey bars show the mean and 95% confidence interval for all trials.

696

697   **Figure 3:** Throughout a saccade, flies produce torque about all body axes, the roll axis, pitch

698   axis, and yaw axis. The total normalized body torque (A-C) is the sum of torques required to

699   resist aerodynamic damping (D-F) and to resist inertia (G, H). All torques are defined in the body

700   reference frame (Figure 1C) and normalized by $|\boldsymbol{a+g}|ml$. Grey lines show data from the separate

701   saccades, black lines with grey bars are means and 95% confidence intervals for all trails.

702

703   **Figure 4:** The early stage of a saccade can be separated into two phases, an initial body rotation

704   (-25ms$<t<$-5ms, data in blue) and a counter-rotation (30ms$<t<$60ms, data in orange). During

705   each phase, flies produce torque about two body axes and keep torque about the third orthogonal

706   axis to a minimum. (A) Direction of torque within the stroke plane, μ, throughout the saccade.

707   (B) Vectors depicting orientation and magnitude of torque component within the stroke plane,

708     $T\mu$, during the initial rotation phase (blue) and during the counter-rotation phase (orange) (see

709   (A) for the time windows). The black dashed vectors are mean $T\mu$ for both time windows,

710   defining the primary torque axis ($\mu_1=36°$) and the counter-torque axis ($\mu_2=8°$). Normalized

711   torque vectors are scaled according to the reference vector of 0.01. (C) Torque about the primary

712   torque axes μ_1 ($t<$12.5ms) and the counter-torque axis μ_2 ($t>$12.5ms). (D) Torque about the

713   orthogonal axes $\mu_{1\perp}$ ($t<$12.5ms) and $\mu_{2\perp}$ ($t>$12.5ms). (E) Torque about the yaw axis. (F) Average

714   magnitude of normalized body torque relative to turn angle $\Delta\sigma$ about the μ_1 (blue) and μ_2

715   (orange) axes. (G) Torques about their orthogonal $\mu_{1\perp}$ and $\mu_{2\perp}$ axes. (H) Torque about the yaw

716   axis. All torques are defined in a right-handed reference frame relative to the μ_1, μ_2 and yaw axes

717   and were normalized by $|\boldsymbol{a}+\boldsymbol{g}|ml$. In A, C, D, and E, grey lines show data from all measured

718   saccades, and black lines with grey bars are means and 95% confidence intervals.

719

720   **Figure 5:** The average wing and body kinematics, determined by aligning the wingbeats of all

721   trials relative to the start of each saccade, show that flies produce aerodynamic torques

722   throughout a saccade using small changes in their wing movement patterns. (A) Wingbeat

723   frequency f, (mean and 95% confidence interval). (B) Stroke angle, ϕ, for the left (blue) and right

724   (red) wing. (C) Difference in stroke angle at the end of the downstroke (blue) and upstroke

725   (orange). (D) Deviation angle, γ. (E) Difference in deviation angle amplitude during the

726   downstroke (blue) and upstroke (orange). (F) wing rotation angle, α. (G) Difference in wing

727   rotation angle at mid-downstroke (blue) and mid-upstroke (orange). (H) Normalized stroke-

728   averaged force, $|\boldsymbol{F}|$, based on body accelerations (black trace for mean and grey bar for 95%

729   confidence interval) and based on wing kinematics shown in B, D, and F (green trace). (I-K)

730   Normalized roll torque, T_{roll} (I), pitch torque, T_{pitch} (J), and yaw torque, T_{yaw} (K). Plotting

731   conventions in (I-K) are the same as in H.

732

733   **Figure 6.** Average wing kinematics angles and torque for wingbeats that generate peak torque

734   about the control axes. (A-C) Kinematics angles for the left wing (blue) and for the right wing

735   (red) for strokes that generated peak yaw torque (A), peak μ_1 torque (B), and peak μ_2 torque (C).

736   (D) Normalized yaw torque measured by replaying wingbeat kinematics in panel A (black) and

737   the steady flight kinematics in Fig. 1D (grey) on the robotic fly model. Solid lines are time series

738   throughout the wingbeat, dotted lines are stroke-averaged values. (E) Normalized torque about

739   the μ_1 axis for the kinematics in panel B (blue), normalized torque about the μ_2 axis for the

740   kinematics in C (orange), and torque about the μ_1 and μ_2 axes for the steady flight wingbeat

741   kinematics in Fig. 1D (black and grey, respectively). Note that the black and grey traces are so

742   similar that they appear to be a single line. (F) Normalized torques about the $\mu_{1\perp}$ and $\mu_{2\perp}$ axes,

743   using the color conventions as in E.

744

745   **Figure 7:** Torques derived from body dynamics plotted against stroke-averaged torques

746   measured using a robotic fly. The data are based on a graded series of wing kinematics that range

747   from steady wingbeats to those that produce peak torque about the μ_1, μ_2, and yaw axes as shown

748   in Fig. 6A-C. (A) Comparison of torque about the three principal body axes: yaw (black), roll

749   (red), and pitch (blue), for the kinematics correlated with yaw production. (B) Comparison of

750   torque about the μ_1 (blue), the μ_2 (orange), $\mu_{1\perp}$ (grey), $\mu_{2\perp}$ (also grey), and yaw (black) axes.

751   Positive values are for the kinematics correlated with control of torque about the μ_1 axis;

752   negative values are for the kinematics that controls torque about the μ_2 axis. (C) Torques

753   produced by varying the different wing kinematics parameters correlated with yaw torque control

754   in isolation while maintaining all others at steady flight conditions. The effect of the different

755   parameters is shown in blue (stroke angle, ϕ), magenta (deviation angle γ), and green (rotation

756   angle α). The grey trace is the sum of the torques for the separate cases; the red trace shows the

757   case where all kinematics angles were varied together. The thin black solid line in all panels

758   shows a match between torques determined from body dynamics and from wing kinematics

759   played through the robot. (D) The same analysis as in C, but using the kinematics correlated

760   with the control of torque about the μ_1 axis (positive values) and the μ_2 axis (negative values).

761

762   **Figure 8:** Flies modulate the phase of wing rotation to control torque about the μ_1 and μ_2 axes,

763   and modulate both the phase and offset of wing rotation to control torque about the yaw axis. (A)

764   Wing rotation angles of the right wing (red), left wing (grey), and left wing trace (blue dotted)

765   that has been translated along both abscissa (wingbeat phase) and ordinate (rotation angle) to

766   produce the lowest RMSE between the right and shifted left wing traces. (B) A plot of RMSE as

767   a function of plot of wingbeat phase ($-10°<\Delta\tau<10°$) and mean wing rotation angle

768   ($-10°<\Delta\alpha<10°$) for the kinematics correlated with peak yaw torque. Maximum correlation

769   (minimum RMSE) is depicted by a white dot. RMSE is coded in grey on a logarithmic scale. (C

770   and D) The same analysis as in A and B, but for the data correlated with peak torque about the μ_1

771   axis. (E and F) The same analysis as in A and B, but for the data correlated with peak torque

772   about the μ_2 axis.

773   <div align="center">**Supplementary Figure Legends**</div>

774   **Figure S1:** Temporal dynamics of body rotations throughout the saccadic maneuver. Rotational

775   dynamics of the fly body are described as angular positions (A-C), normalized angular velocities

776   (D-F) and normalized angular accelerations (G-I) about the principal body axes (roll axis, pitch

777   axis and yaw axis as defined in Fig. 1C). The temporal dynamics of the angular positions were

778   estimated by integrating angular velocities in the body reference frame (integration constant was

779   set to zero at the start of each track); angular velocities were normalized by the wingbeat

780   frequency at steady flight, f_{steady}, estimated by Muijres et al. (2014); angular accelerations were

781   estimated by differentiating angular velocities, and were normalized by the steady wingbeat

782   frequency f^2_{steady}. Grey lines show data from all measured saccades, and black lines with grey

783   bars are means and 95% confidence intervals for all trails.

784

785 **Figure S2:** Torque dynamics within the stroke plane throughout the saccadic maneuver,

786 described by torque about the primary torque axis μ_1 (A), the counter-torque axis μ_2 (B) and their

787 respective orthogonal axes $\mu_{1\perp}$ (C) and $\mu_{2\perp}$ (D). All torques are normalized by $|a+g|ml$; grey

788 lines show data from the separate saccades, and black lines with grey bars are means and 95%

789 confidence intervals for all trails. The vertical dotted line defines the point in time where torque

790 in the stroke plane is approximately zero, and that therefore separates the primary rotation phase

791 and the counter-rotation phase (t=12.5 ms).

792

793 **Figure S3:** Correlation between wingbeat kinematics angles of the left and right wing, for the

794 kinematics that results in peak yaw torque (left column), peak torque about the primary μ_1 axis

795 (middle column), and peak torque about the counter-torque axis μ_2 (right column). (A-C)

796 kinematics angles of the right wing (red), the original kinematics of the left wing (grey), and the

797 translated left wing kinematics for which correlation between the wingbeat kinematics angles of

798 the left and right wing were maximal (blue dotted traces). (D-L) root-mean square error (RMSE)

799 based on the difference between the left and right wing kinematics angle throughout the

800 measured phase shift range $-10°<\Delta\tau<10°$ and mean kinematics angle shift range $-10°<\Delta\kappa<10°$

801 (maximum correlation at minimum RMSE is depicted by a white dot): (D-F) for stroke angle;

802 (G-I) for deviation angle; (J-L) for wing rotation angle. Logarithmic values of RMSE are scaled

803 according to the scale bar in (L).

804 **Supplementary Movie Legends**

805 **Movie S1:** Top view of a fruit fly performing a saccadic maneuver. The movie is slowed down

806 100 times, and every third recorded frame is shown. The turn angle of this saccade is

807 approximately 90 degrees, which is close to the average saccadic turn angle for all trails.

808

809 **Movie S2:** Body and wings model of a fruit fly performing a saccadic maneuver. The movie is

810 slowed down 300 times. The turn angle of this saccade is approximately 90 degrees, which is

811 close to the average saccadic turn angle for all trails.

812

813 **Movie S3:** A movie of all 44 flight tracks overlaid on top of each other, viewed from below. The

814 movie is slowed down 100 times, and traces are color-coded with time according to the scale bar

815 in Fig. 1E. Note that all left-handed turns have been mirrored into right-handed turns, and all

816 sequences were aligned according to position and heading at the start of the saccadic maneuver
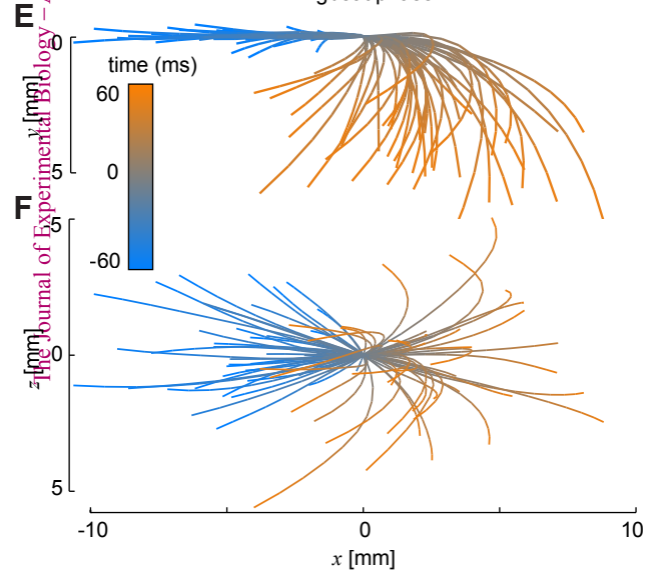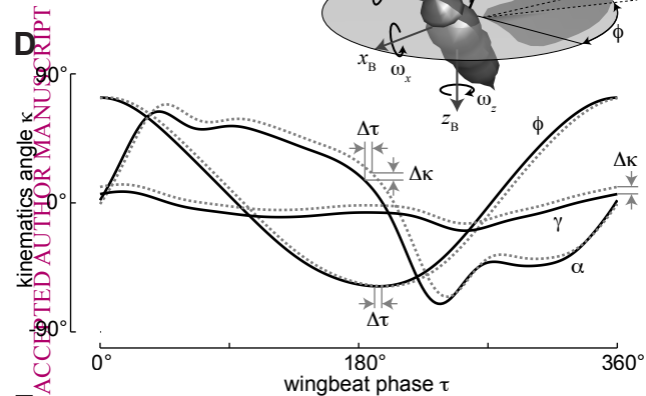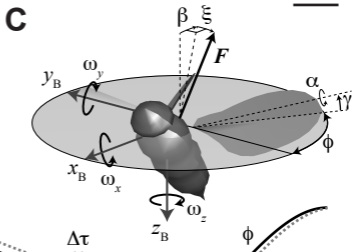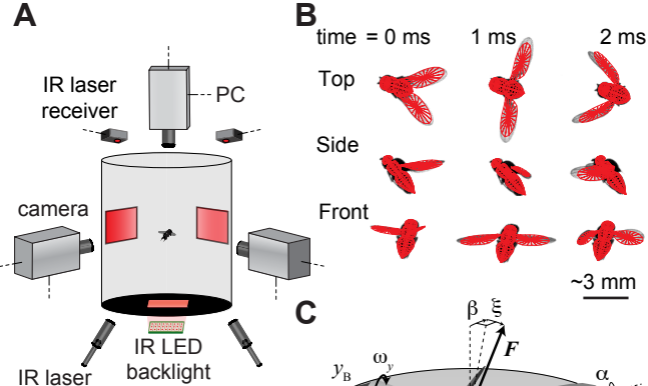
817 (t_{start} = 0 ms).

818

819 **Movie S4:** A movie of all 44 flight tracks overlaid on top of each other, viewed from the side as

820 shown in Fig. 1F. The movie is slowed down 100 times, and traces are color-coded with time

821 according to the scale bar in Fig. 1E. Note that all left-handed turns have been mirrored into

822 right-handed turns, and all sequences were aligned according to position and heading at the start

823 of the saccadic maneuver (t_{start} = 0 ms).
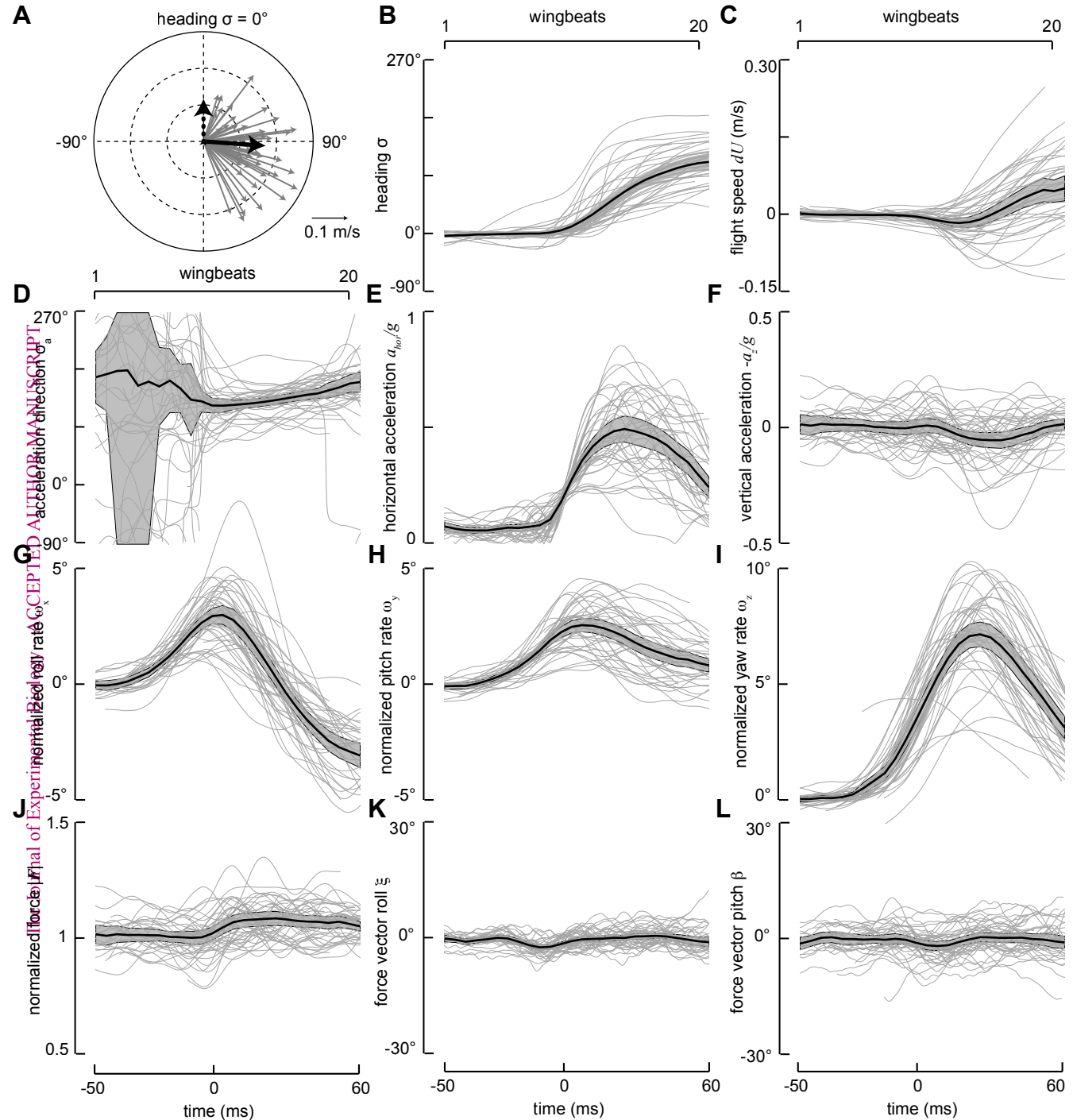
824

825 **Movie S5:** A movie of all 44 flight tracks overlaid on top of each other, viewed from the front.

826 The movie is slowed down 100 times, and traces are color-coded with time according to the scale

827 bar in Fig. 1E. Note that all left-handed turns have been mirrored into right-handed turns, and all

828   sequences were aligned according to position and heading at the start of the saccadic maneuver

829   ($t_{start} = 0$ ms).

830

831   **Movie S6:** A movie of all 44 flight tracks overlaid on top of each other, in perspective view. The

832   movie is slowed down 100 times, and traces are color-coded with time according to the scale bar

833   in Fig. 1E. Note that all left-handed turns have been mirrored into right-handed turns, and all

834   sequences were aligned according to position and heading at the start of the saccadic maneuver
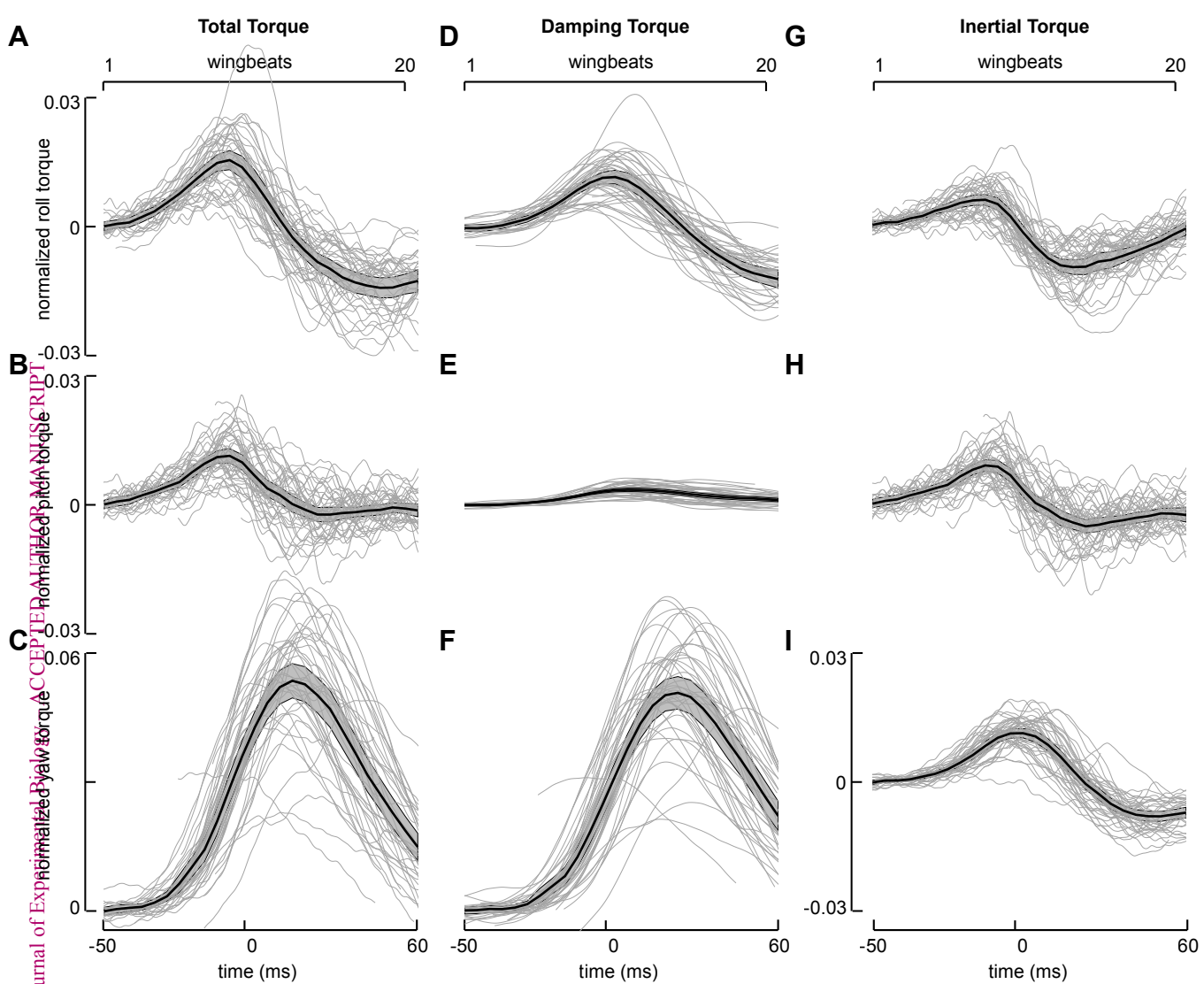
835   ($t_{start} = 0$ ms).

A
IR laser receiver — PC
camera
IR laser
IR LED backlight

B
time = 0 ms   1 ms   2 ms
Top
Side
Front
~3 mm

C
β ξ
y_B ω_y F α
x_B ω_x φ
z_B ω_z γ

The Journal of Experimental Biology – ACCEPTED AUTHOR MANUSCRIPT

Left margin text (rotated): The Journal of Experimental Biology – ACCEPTED AUTHOR MANUSCRIPT

Figure axis labels:

A — rotation angle α, $90°$, $0°$, $-90°$
B — rotation angle shift $\Delta\alpha$, $10°$, $0°$, $-10°$; log(RMSE), 2, 0
C — rotation angle α, $90°$, $0°$
D — rotation angle shift $\Delta\alpha$, $10°$, $0°$, $-10°$
E — rotation angle α, $90°$, $0°$, $-90°$; wingbeat phase τ, $0°$, $360°$
F — rotation angle shift $\Delta\alpha$, $10°$, $0°$, $-10°$; phase shift $\Delta\tau$, $-10°$, $0°$, $10°$